Journal of Alloys and Compounds 1062 (2026) 187599

Contents lists available at ScienceDirect

Journal of Alloys and Compounds

journal homepage: www.elsevier.com/locate/jalcom

Strengthening of an Fe-C-Cr-Ni hypoeutectic alloy by rapid solidification under additive manufacturing conditions and further strengthening by post heat treatment

Kiyotaka Matsuura [a,d,*], Genki Saito [b,1], Norihito Sakaguchi [a], Naomi Kitagawa [c], Pawe Rutkowski [d], Dariusz Kata [d]

[a] Faculty of Engineering, Hokkaido University, Kita 13 Nishi 8, Kita-ku, Sapporo, Hokkaido 060-8623, Japan
[b] Graduate School of Engineering, Nagoya University, Furo-cho, Chikusa-ku, Nagoya, Aichi 464-8603, Japan
[c] Research and Development Center, Mitsubishi Steel MFG. Co., Ltd., 1-6 Yawata Kaigandori, Ichihara, Chiba 290-0067, Japan
[d] Faculty of Materials Science and Ceramics, AGH University of Krakow, al. Mickiewizca 30, Cracow 30-059, Poland

ARTICLE INFO

Keywords:
Interparticle distance
Eutectic particles
Chromium carbide
Dendrite arm spacing
Hall-Petch law
Precipitation hardening

ABSTRACT

This paper investigates the effects of γ-Fe dendrite arm spacing and inter-dendritic eutectic Cr_7C_3 particle spacing on the hardness of an as-solidified hypoeutectic alloy (Fe-2.14mass%C-32.38mass%Cr-6.48mass%Ni-0.90mass% Si), as well as the effects of subsequent heat treatment on the hardness. When the cooling rate was varied between 10^4 and 10^7 °C/s, the hardness of the as-solidified alloy increased exponentially with decreasing dendrite arm spacing and eutectic particle spacing. When this alloy was subjected to laser powder bed fusion (LPBF) process, the hardness exceeded 700 HV, more than twice that of Inconel 718 Ni-based superalloy fabricated using the same process. During subsequent heat treatment at 800 °C, extremely fine $Cr_{23}C_6$ particles precipitated in both the γ-Fe dendrite arms and the γ-Fe matrix phase of the eutectic structure, increasing the hardness of the alloy samples. Although the initial hardness of the dendrite arms was lower than that of the eutectic region, the increase in hardness was greater in the dendrite arms, indicating greater precipitation hardening in the dendrite arms than in the eutectic region. The average hardness of a large arear of the hypoeutectic structure, consisting of dendrites and eutectic regions, was always higher in the heat-treated samples with higher cooling rates during solidification. This is due to the higher supersaturation of Cr and C during cooling, which resulted in a higher number density and volume fraction of $Cr_{23}C_6$ particles precipitated in the γ-Fe.

1. Introduction

Ni-based superalloys have excellent mechanical and chemical properties [1,2], and are widely used in various industries, including aerospace and automotive industries [3,4]. However, due to their high Ni content, these alloys are significantly more expensive than other alloys. The development of high-strength Fe-based alloys with reduced Ni content is expected to contribute to reducing material costs in many industries.

The present authors have recently developed an Fe-C-Cr-Ni eutectic alloy and applied it to a Laser Powder Bed Fusion (LPBF) process to fabricate a small prototype. The as-built prototype exhibited a significantly high hardness of ~720 HV, which is twice as hard as an Inconel 718 Ni-based superalloy sample fabricated using the same process [5]. Generally, the finer the solidification structure, the higher the mechanical strength of the as-solidified alloy [6]. However, the as-built Inconel 718 alloy fabricated by LPBF exhibited a hardness of only ~350 HV, despite having an extremely small primary dendrite arm spacing of less than 1 μm [5]. In typical casting processes, the primary dendrite arm spacing indirectly determines the grain size due to the heterogeneous nucleation of dendrite crystals [7]. However, in LPBF and other additive manufacturing processes, such as Directed Energy Deposition (DED), the molten pool formed by the laser beam partially melts the previously solidified molten pool and solidifies epitaxially at the solid/liquid interface, resulting in the formation of a huge grain structure despite the fine dendritic structure [8]. Therefore, Hall-Petch

* Corresponding author at: Faculty of Engineering, Hokkaido University, Kita 13 Nishi 8, Kita-ku, Sapporo, Hokkaido 060-8623, Japan.
E-mail address: dc_matsu@outlook.jp (K. Matsuura).
1 Present address: School of Engineering, The University of Shiga Prefecture, Hassaka-cho 2500, Hikone, Shiga 522-8533, Japan.

https://doi.org/10.1016/j.jallcom.2026.187599
Received 29 January 2026; Received in revised form 20 March 2026; Accepted 24 March 2026
Available online 27 March 2026
0925-8388/

Table 1
Dimensions and cooling rates of samples.

Samples	Dimension (mm)	Cooling Rate (℃/s)
Furnace-remelted Ingot	Φ 20 × h 15	2×10^{-1}
Arc-remelted Bead	Φ 6 × d 4	$\sim 10^4$
DED Prototype	50 × 50 × 75	$\sim 10^5$
Laser-remelted zone	l 4 × w 3 × d 0.15	$\sim 10^6$
LPBF Prototype	Φ 10 × t 0.3	$\sim 10^7$

strengthening cannot be expected in conventional alloys like Ni-based superalloy that form dendritic solidification structures during additive manufacturing. In contrast, the LPBF-built Fe-C-Cr-Ni eutectic alloy had an extremely fine eutectic structure consisting of a γ-Fe matrix phase and rod-like chromium carbide particles, with the distance between the eutectic carbide rods being around 70 nm [5]. Due to this short dislocation travel distance in the γ-Fe matrix phase, this alloy exhibited such a high hardness of ~720 HV. This explains why the LPBF-built Fe-C-Cr-Ni eutectic alloy was much harder than the LPBF-built Inconel 718 superalloy.

In our recent study on the Fe-C-Cr-Ni eutectic alloy [5], equilibrium thermodynamic calculations predicted the precipitation of $Cr_{23}C_6$ carbide particles in the γ-Fe matrix phase, but no carbide precipitation was observed in the as-solidified samples. This suggests that the γ-Fe matrix phase is supersaturated with chromium and carbon, and post-solidification heat treatment is expected to introduce the precipitation of $Cr_{23}C_6$ carbide particles, further improving the strength of the alloy. The distance between the precipitated carbide particles will be much shorter than that between the eutectic carbide particles, and the strengthening effect of the former will be much greater than that of the latter. The presence of primary solidified γ-Fe dendrites is predicted to favor the carbide precipitation, as it provides a larger volume of the supersaturated matrix phase. Therefore, in this study, we developed an Fe-C-Cr-Ni hypoeutectic alloy consisting of γ-Fe dendrites and inter-dendritic eutectic chromium carbide particles, and investigated the effects of the cooling rate during solidification and holding time of the post heat treatment on hardness. One will see that the heat treatment is effective in increasing the hardness and the increased hardness is always higher in the samples with the finer solidification structure even after heat treatment.

2. Experimental procedure

The chemical composition of this hypoeutectic alloy was determined based on a calculated equilibrium phase diagram [5]. The alloy powder was then produced using a gas atomization process (Mitsubishi Steel MFG. Co., Ltd.). Analysis of the alloy powder revealed its chemical composition to be Fe-2.14mass%C-32.38%massCr-6.48mass%Ni-0.90mass%Si. Based on this analyzed composition, the equilibrium temperature-volume fraction relationships of the phases in this alloy were calculated using Thermo-Calc software (version 2024) and the latest version of database (TCFE14, 2025).

Five types of samples were prepared using five different methods with cooling rates ranging from 2×10^{-1} to $\sim 10^7$ °C/s, as summarized in Table 1. The details of the preparation of the five types of samples are as follows. **(i)** The alloy powder was remelted in an alumina crucible under an Ar atmosphere and cooled at a rate of 0.2 °C/s to obtain a small ingot with a diameter of 20 mm and a height of 15 mm. **(ii)** On the side surface of this ingot, small beads with a diameter ~6 mm and a depth ~3 mm were created by applying a short-time arc discharge using a TIG welding machine (YC-200TR6, Panasonic) under an Ar shielding gas atmosphere. The TIG arc discharge was performed under the following conditions: voltage, DC current, and discharge time were 10 V, 10 A and 2 s, respectively. The cooling rate of the arc-remelted beads was estimated to be $\sim 10^4$ - $\sim 10^5$ °C/s based on the relationship between secondary dendrite arm spacing and cooling rate [9]. **(iii)** A prototype with a dimension of 50 × 50 × 70 (mm) was fabricated from the alloy powder

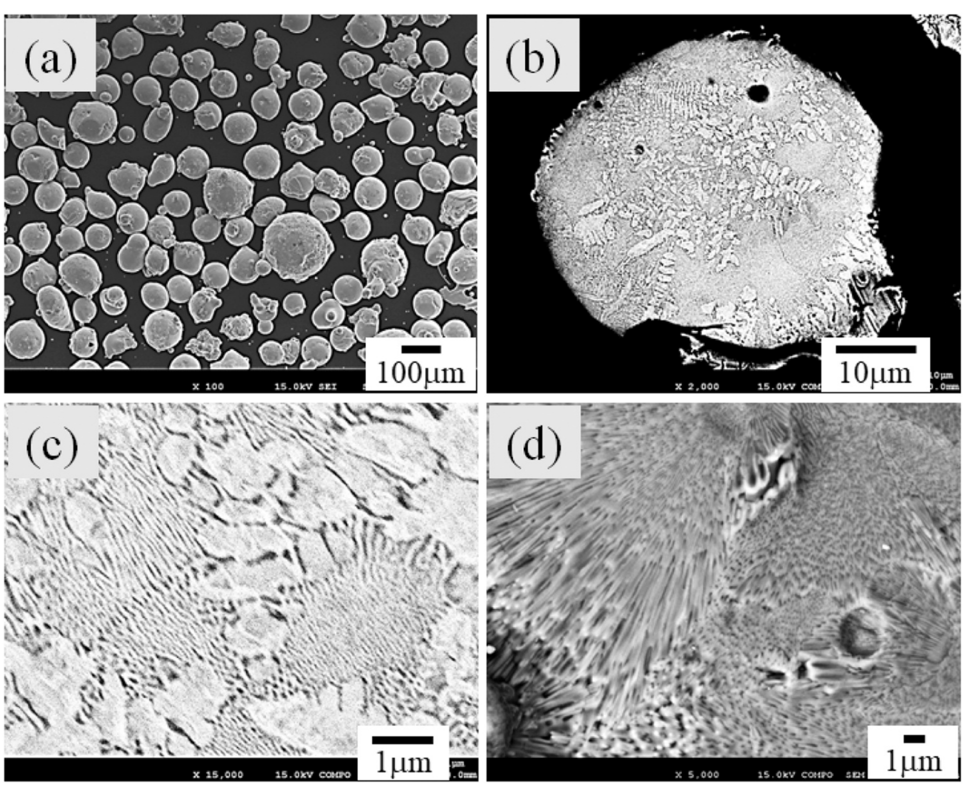

Fig. 1. SEM images of the gas-atomized powder. (a) appearance of powder particles, (b) a cross section of a powder particle showing the distribution of primary-solidified dendrites, (c) a cross section of a powder particle showing eutectic structures formed in inter-dendritic regions, and (d) the surface of a powder particle showing rod-like eutectic morphology.

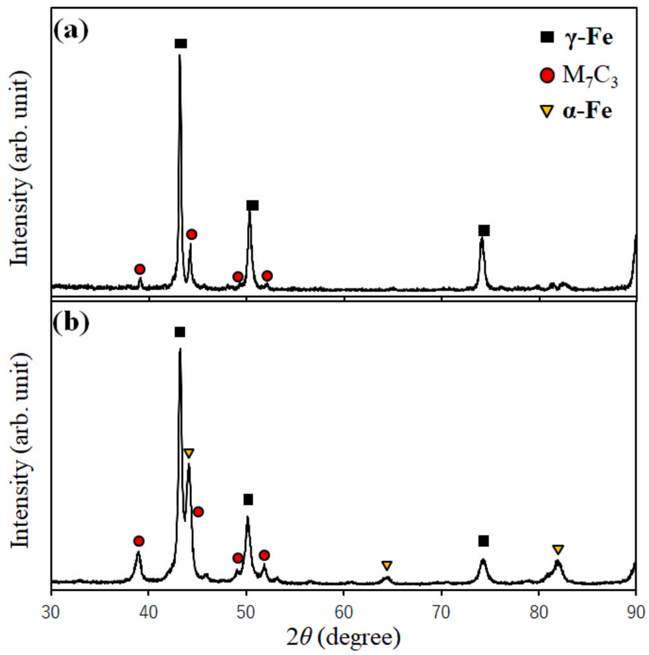

Fig. 2. XRD analysis results of (a) the as-atomized alloy powder and (b) the as-solidified furnace-remelted ingot.

using the DED (Directed Energy Deposition) process. DED was performed in an Ar atmosphere using a DED system (LASER TEC 65 3D Hybrid, DMG MORI) under the following conditions: laser power 2000 W, laser nozzle diameter 3 mm, nozzle scan speed 1000 mm/s, powder feed rate 12.5 g/min, carrier gas flow 3 L/min, and shield gas flow 5 L/min. The cooling rate of the molten pool was estimated to be ~10^5 - ~10^6 °C/s based on the secondary dendrite arm spacing. **(iv)** On a vertical cross section of the DED prototype, small molten zones of ~4 mm long, ~3 mm wide, and 0.15 mm deep were created by laser beam scanning using a laser scanner (JK200FL of JK Lasers a GSI Group Company, hurrySCAN 30 of SCANLAB) with CW (Continuous Wave) operating mode under an Ar atmosphere. The laser scanning was performed under the following conditions: power 200 W, scan speed 50 mm/s, and spot diameter 40 μm. The formation of the molten pool was repeated at 40 μm intervals to create the molten zone. The cooling rate of the molten pool was estimated to be ~10^6 - ~10^7 °C/s based on the secondary dendrite arm spacing. **(v)** A prototype with a diameter of 10 mm and a thickness of 0.3 mm was fabricated from the alloy powder using the LPBF (Laser Powder Bed Fusion) process. LPBF was performed using a LPBF system (TruPrint 1000, TRUMPF) in an Ar gas atmosphere under the following conditions: laser power of ~60 to ~115 W, laser spot diameter of 55 μm, and laser scan speed of ~400 to ~700 mm/s. The cooling rate of the molten pool was estimated to be ~10^7 °C/s based on an experimental result [10].

The samples fabricated using above methods were heat-treated at 800 °C for 0.5–64 h in an Ar atmosphere. The heating and cooling rates were 0.2 °C/s. Microstructures of the samples were observed using Optical Microscopy (OM, VHX-6000, Keyence), Scanning Electron Microscopy (SEM, Phenom ProX, Thermo Fisher Scientific), and Scanning Transmission Electron Microscopy (STEM, NEOARM, JEOL). X-ray diffraction analysis (XRD, Ultima IV , Rigaku) using Cu Kα radiation (1.54056 nm in wavelength) was performed at room temperature and elevated temperatures to identify the phases present in the alloy samples. A Vickers hardness tester (FM-300e, FUTURE-TECH) was used with an applied load between 0.05 and 1.00 kg depending on the microstructural fineness. Five indentations were made to obtain the average hardness of each sample. Samples were prepared by cutting with a diamond wheel, grinding with emery paper, and polishing with colloidal silica (particle diameter 0.05 μm), and then subjected to OM and SEM observations and hardness tests. For STEM observations, samples were prepared using an FIB (Focused Ion Beam, JEM-9320, JEOL). The dendrite arm spacing, eutectic particle spacing, and number density and area fraction of precipitated particles were measured inside or near the Vickers indentation to investigate their relationships with hardness.

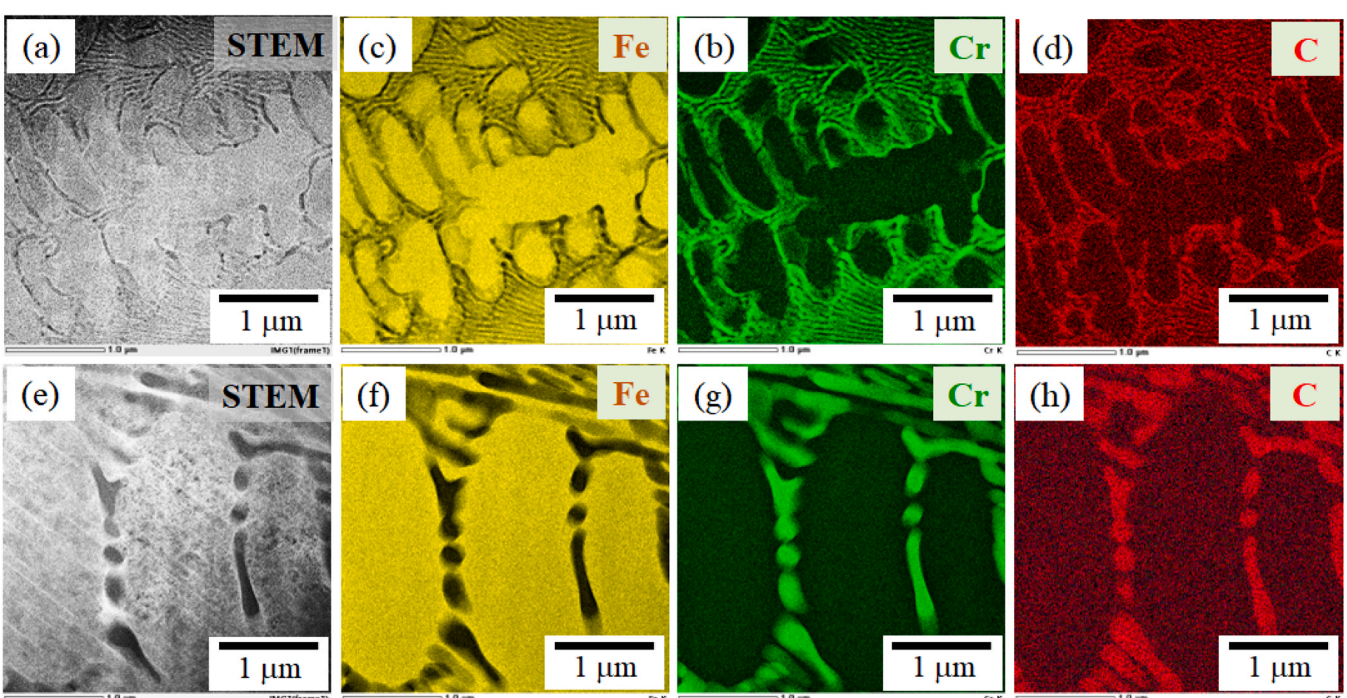

Fig. 3. STEM-EDS analysis results of (a-d) the laser-remelted zone and (e-h) the DED prototype, showing that γ-Fe dendrite arms contain no carbide precipitates and that the inter-dendritic region is filled with a dual-phase structure consisting of rod-like eutectic chromium carbide particles and Fe matrix phase.

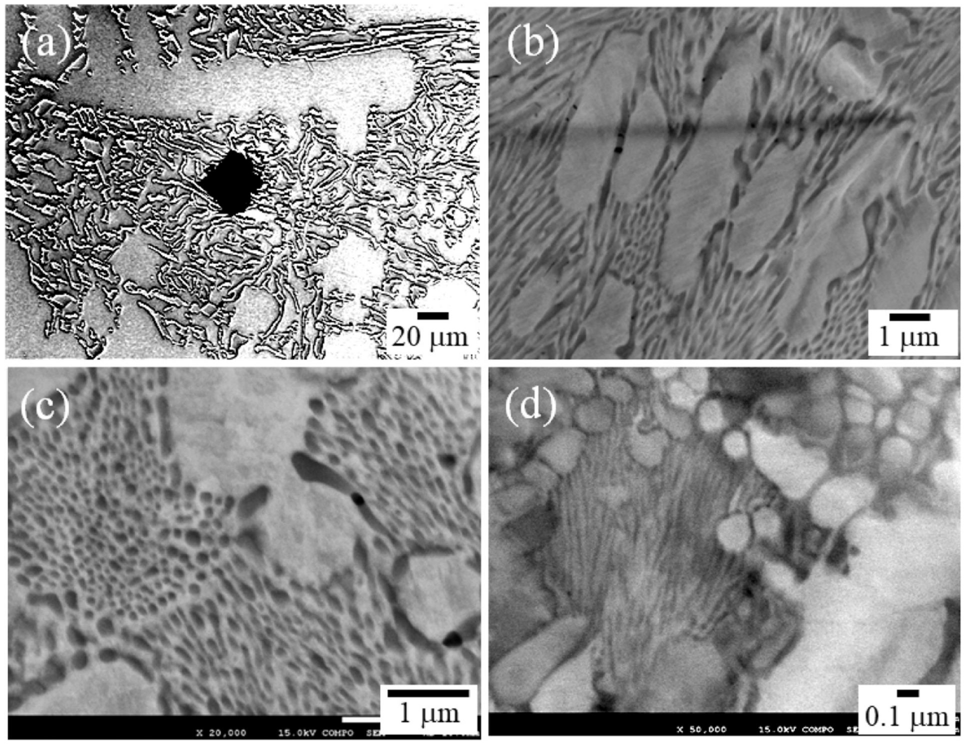

Fig. 4. Solidification structures of (a) furnace-remelted ingot, (b) arc-remelted bead, (c) DED prototype, and (d) LPBF prototype. The square mark in (a) is a Vickers indentation.

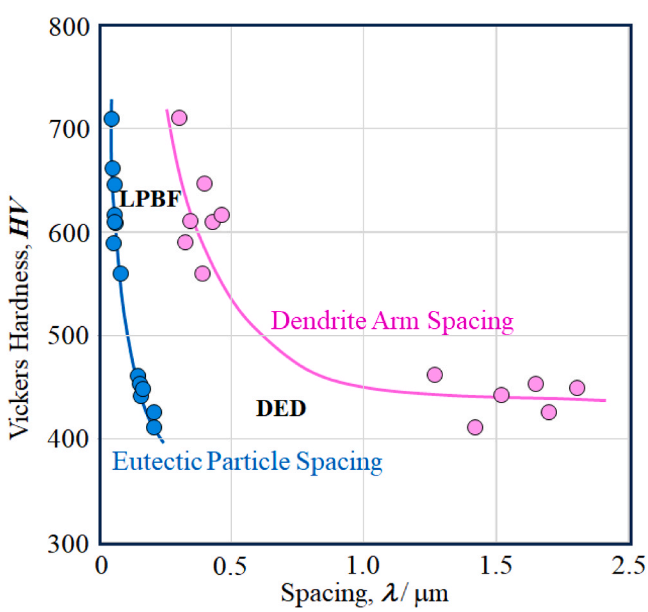

Fig. 5. Effects of secondary dendrite arm spacing and eutectic particle spacing on Vickers hardness measured on as-built DED and LPBF prototypes.

3. Results and discussion

3.1. Effects of solidification structure

Fig. 1 shows SEM images of the gas-atomized alloy powder. The powder particles are spherical and ~50 to ~100 µm in diameter (Fig. 1**(a)**). The solidification structure consisted of dendrites and fine dual-phase structures (Figs. 1**(b)** and 1**(c)**). The particles in the dual-phase structure have a rod-like morphology (Fig. 1**(d)**). In order to identify the phases existing in the powder, XRD analysis was performed at room temperature. The result shown in Fig. 2**(a)** indicates that the as-atomized powder is composed exclusively of γ-Fe and M_7C_3-type carbide, which reveals that the rod-like particles seen in Fig. 1 are Cr_7C_3 and the matrix phase including dendrites is γ-Fe. However, the as-solidified furnace-remelted ingot produced using this powder consisted of γ-Fe, M_7C_3-type carbide, and a certain amount of α-Fe, as shown in Fig. 2**(b)**. This means that the γ-to-α transformation partially occurred during slow cooling in the furnace, but the transformation did not occur during powder atomization due to the extremely rapid cooling. Results of STEM-EDS analysis, shown in Fig. 3, reveal that the dendrites are composed of Fe, with eutectic chromium carbide particles in the interdendritic regions, a typical solidification structure for hypoeutectic alloys. It should be noted that the Fe dendrites in the as-solidified samples were free of precipitates.

Fig. 4 shows examples of solidification structures of samples fabricated using different methods. The furnace-remelted ingot sample (Fig. 4**(a)**) has coarse dendrites and large eutectic carbide particles, whereas the samples fabricated at much higher cooling rates (Figs. 4**(b)**-4**(d)**) have much smaller dendrites and extremely fine rod-like eutectic particles (Note the difference in scale bars). No precipitates were observed in the Fe dendrite arms even in the sample fabricated at the slowest cooling rate of 0.2 ^{o}C/s.

Vickers hardness measurements were performed on as-built samples of the DED and LPBF prototypes, and secondary dendrite arm spacing and eutectic particle spacing were measured inside or near each indentation to investigate the effects of these two spacings on hardness. The results are summarized in Fig. 5. As these two spacings decreased, hardness increased exponentially to over 700 HV, more than twice that

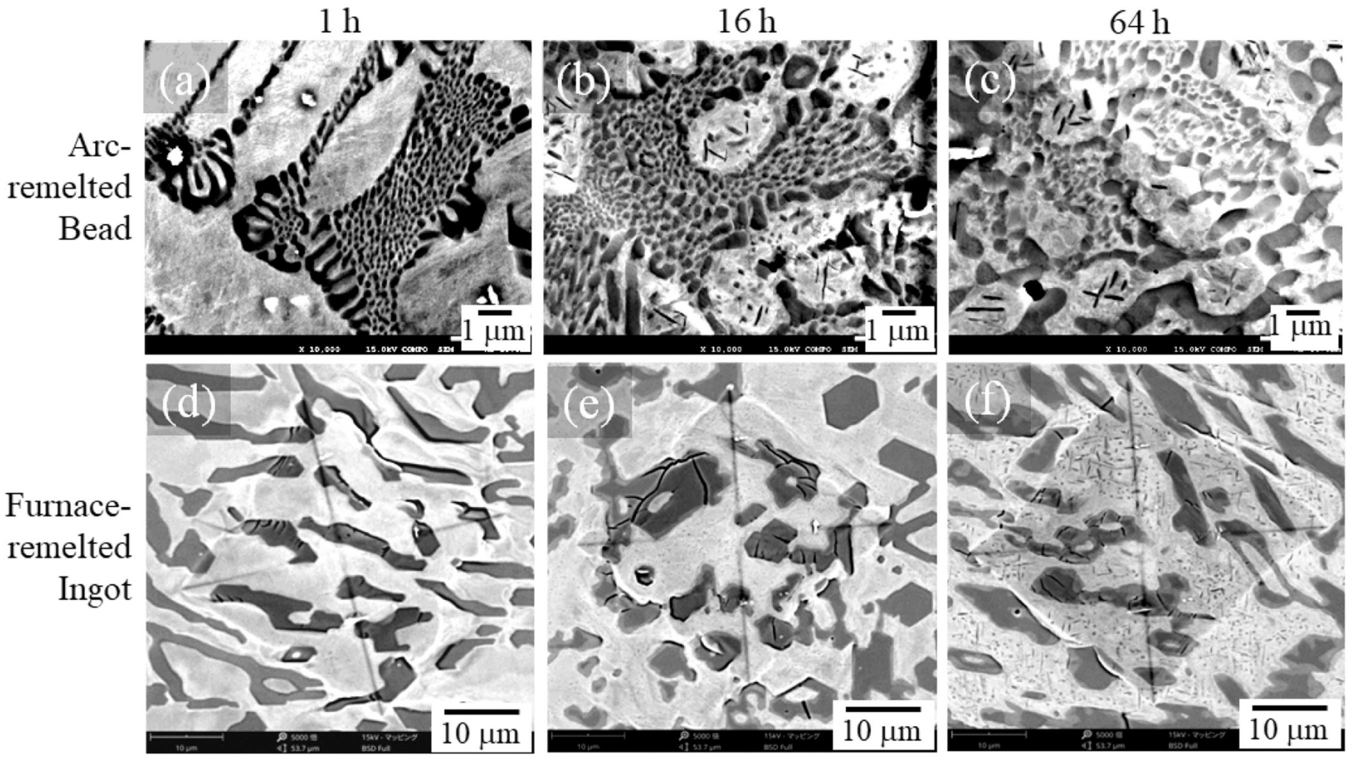

Fig. 6. SEM images of heat-treated samples, held at 800 °C for (a, d) 1 h, (b, e) 16 h, (c, f) 64 h, showing (a-c) dendrites and inter-dendritic eutectic regions of the arc-remelted bead, and (d-f) eutectic regions of the furnace-remelted ingot. The large squares with diagonal lines seen in (d) to (f) are Vickers indentations.

of Inconel 718 Ni-based superalloy fabricated using LPBF process [11]. The effect of eutectic particle spacing on hardness was stronger than that of secondary dendrite arm spacing. Both spacings decrease with increasing cooling rate. However, the mechanisms by which cooling rate affects the two spacings are different. As cooling rate increases, secondary dendrite arm spacing decreases due to decreased diffusion time, while eutectic particle spacing decreases due to increased nucleation frequency caused by increased supercooling, as well as decreased diffusion time.

3.2. Effects of heat treatment

Fig. 6 shows microstructures of the heat-treated samples of the arc-remelted bead (Figs. 6**(a)** to 6**(c)**) and the furnace-remelted ingot (Figs. 6**(d)** to 6**(f)**). With increasing holding time, the eutectic carbide particles in both the bead and ingot became larger and more spheroidized, indicating that Ostwald ripening occurred during heat treatment. Ostwald ripening of the inter-dendritic eutectic carbide particles resulted in an irregular dendritic structure (Fig. 6**(c)**). In the arc-remelted bead samples held for 16 and 64 h (Figs. 6**(b)** and 6**(c)**), needle-like particles are observed in the Fe dendrite arms. Similar needle-like particles were also observed in the Fe dendrite arms of the furnace-remelted ingot, and they grew during the heat treatment, as shown in Fig. 7**(a)** to **(d)**. Extremely small dark dots are observed in the Fe matrix phase of the eutectic region of the furnace-remelted ingot sample held for 64 h (Fig. 6 **(f)**), and when observed under higher magnification, they were also found to have a needle-like morphology (Fig. 7**(f)**). The needle-like particles precipitated over a wide area within the Fe dendrites, and showed a regular distribution pattern indicating nucleation on specific crystallographic planes, suggesting that the formation of the needle-like particles occurred mainly via intragranular nucleation.

These needle-like particles are considered to be $Cr_{23}C_6$ precipitates based on the XRD analysis results shown in Fig. 8 and the equilibrium phase diagram calculations shown in Fig. 9. Before heat treatment, no needle-like precipitates were observed (Figs. 3 and 4), and no $Cr_{23}C_6$ was detected (Fig. 8**(a)**). However, after heat treatment, the needle-like precipitates were observed (Figs. 6 and 7), and only $M_{23}C_6$ type carbide was detected (Fig. 8**(b)**). This means that $Cr_{23}C_6$ particles nucleated and grew, and the eutectic Cr_7C_3 particles transformed into $Cr_{23}C_6$ during heat treatment. The phase diagram calculation results indicated that Cr_7C_3 completely transforms into $Cr_{23}C_6$ at the heat treatment temperature of 800 °C.

Thus, both heat treatment experiments and theoretical calculations under the equilibrium condition indicated that $Cr_{23}C_6$ is more stable than Cr_7C_3 at the heat treatment temperature and at lower temperatures including room temperature. However, in the samples continuously cooled after solidification, only Cr_7C_3 carbide was detected at room temperature, which means that Cr_7C_3 carbide exits in a metastable state and formation of $Cr_{23}C_6$ during cooling is hard. We performed a simple experiment to promote the formation of $Cr_{23}C_6$ carbide. We reheated the as-built DED sample to 800 °C at 0.7 °C/s and cooled it to room temperature at the same rate, and we performed continuous XRD analysis during this thermal cycle. We detected α-to-γ transformation during reheating and γ-to-α transformation during cooling, but Cr_7C_3 carbide remained stable throughout and no $Cr_{23}C_6$ was detected by the continuous XRD analysis. Therefore, Cr_7C_3 carbide exits in a metastable state during and after cooling in the as-solidified alloy. Upon heat treatment, it gradually transforms into $Cr_{23}C_6$ and precipitates from the Fe matrix.

Vickers hardness measurements were performed on the Fe dendrite regions of the furnace-remelted ingot samples, and the area fraction and number density of $Cr_{23}C_6$ particles dispersed in the Fe dendrite region were measured inside or near each indentation. The results are

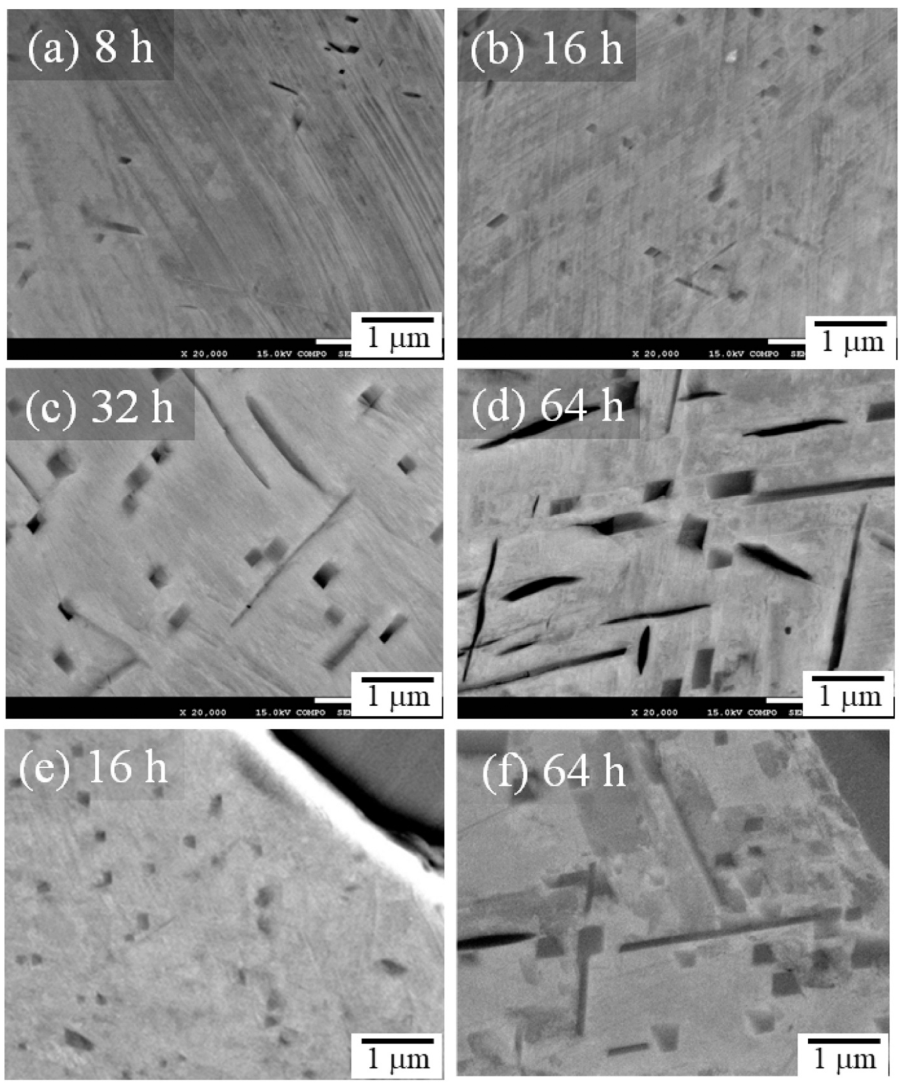

Fig. 7. SEM images of the furnace-remelted ingot, showing carbide precipitates formed during heat treatment (a-d) in the Fe dendrite and (e, f) in the Fe matrix phase of the inter-dendritic eutectic region.

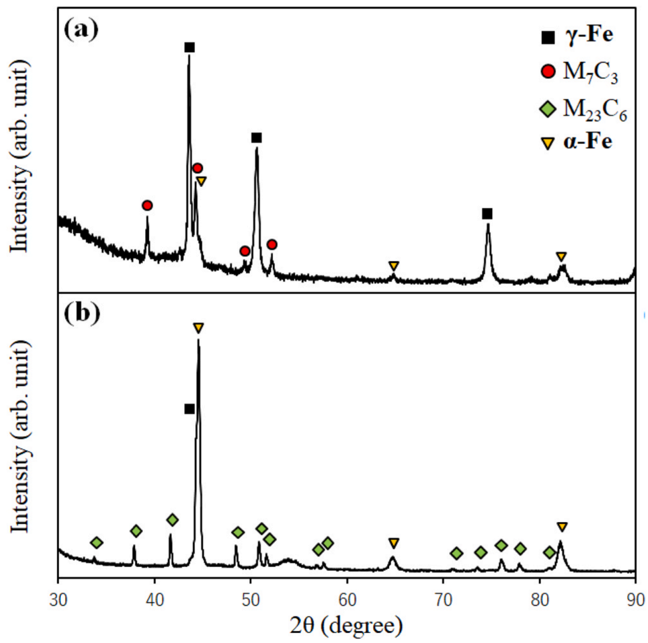

Fig. 8. XRD results of the DED prototype: (a) before and (b) after heat treatment for 64 h at 800 °C.

summarized in Fig. 10. Fig. 10**(a)** shows the increase in the area fraction and number density of $Cr_{23}C_6$ particles in the Fe-dendrite region during heat treatment of the furnace-remelted ingot. While the area fraction gradually increased, the number density increased sharply in the beginning of heat treatment and then showed little increase, suggesting that the concentrated nucleation of $Cr_{23}C_6$ particles occurred in the early stage of heat treatment, followed by gradual particle growth. Due to this precipitation behavior, as shown in Fig. 10**(b)**, hardness increased rapidly in the early stage of heat treatment and then gradually increased.

Fig. 11 shows the relationship between eutectic Cr_7C_3 particle spacing and hardness for the heat-treated furnace-remelted ingot samples and arc-remelted bead samples. The eutectic particle spacing was measured inside or near each indentation. A nearly linear relationship was observed between the inverse square root of eutectic particle spacing and the hardness, indicating that the Hall-Petch law still holds to this hypoeutectic alloy even after heat treatment. This means that the hardness of this alloy is predominantly controlled by the distribution of eutectic Cr_7C_3 particles, regardless of the presence of the Fe dendrites containing fine $Cr_{23}C_6$ precipitates. The influence of $Cr_{23}C_6$ particle precipitation in the Fe matrix on hardness can be seen in the change in the slope and the *y*-intercept of the linear relationship. For both the furnace-remelted ingot and arc-remelted bead samples, hardness increases with increasing holding time. However, the increase in hardness is more pronounced for the arc-remelted bead sample, indicating a stronger effect of precipitation in finer solidification structure. As the holding time increases, the plot marks of the arc-remelted bead sample shift to the left, indicating an increase in the eutectic particle spacing due to the Ostwald ripening, as seen in Figs. 6**(a)** to 6**(c)**.

The effects of heat treatment on hardness are summarized in Fig. 12. Although only average values are shown in the figure, the data error ranged from 2.1% to 21.0%. Large error occurred in the furnace-remelted ingot sample, which is likely due to the coarse solidification structure. Although there is some degree of error, Fig. 12 clearly shows how the holding time affects the hardness of different samples fabricated using different processes. The laser-remelted zone formed on the surface of the DED prototype exhibited the highest hardness, rapidly increasing from ~530 HV to ~670 HV as the holding time increases to 4 h, and then gradually decreasing to ~630 HV. The DED prototype and the arc-remelted bead exhibited similar hardening behaviors, with hardness rapidly increasing from ~450 HV to ~560 HV in the early stage of the heat treatment, and then gradually increasing to ~620 HV. The hardness of the eutectic region of the furnace-remelted ingot increased slowly from ~ 400 HV, reaching ~485 HV in 64 h. Thus, the increase in hardness during heat treatment was greater when the cooling rate during solidification was higher. Rapid cooling increases the degree of supersaturation of chromium and carbon in Fe-matrix phase, resulting in an increase in the number density and volume fraction of $Cr_{23}C_6$ particle precipitates. This is considered to be the reason why the laser-remelted zone exhibited the highest hardness. In fact, the $Cr_{23}C_6$ particles formed in the Fe dendrites of the laser-remelted zone (Figs. 13**(a)** to 13 **(d)**) are extremely small and distributed in high number density compared with those in the DED prototype (Figs. 13**(e)** to 13 **(h)**) and the furnace-remelted ingot (Figs. 6**(b)** and 6**(c)**).

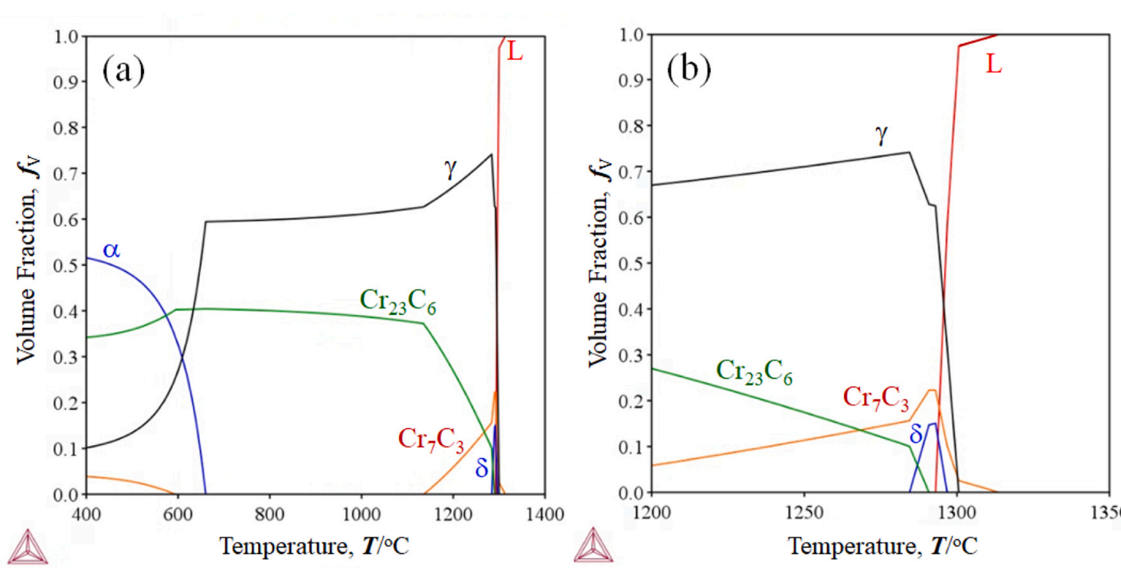

Fig. 9. Equilibrium temperature-volume fraction relationships of the phases existing in the present hypoeutectic alloy. A high-temperature part of (a) is enlarged and depicted in (b).

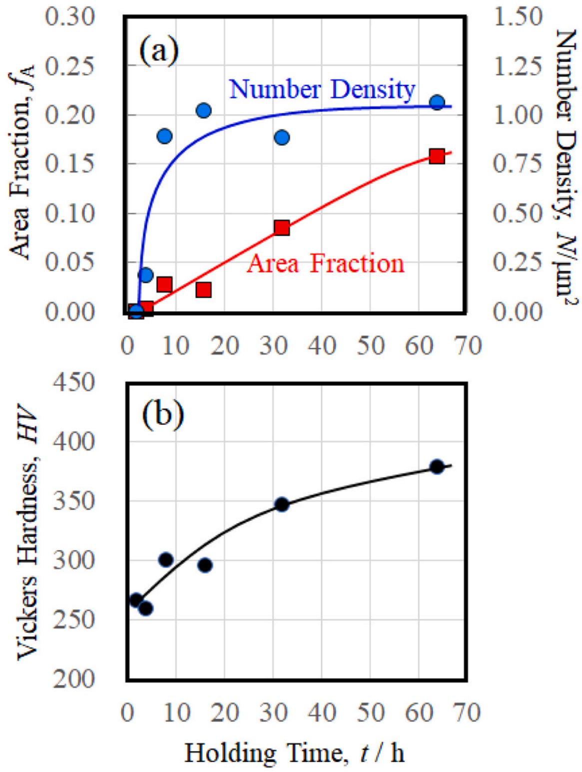

Fig. 10. Increases in (a) area fraction and number density of carbide precipitates formed in the Fe dendrite region during heat treatment of the furnace-remelted ingot, and (b) hardness of the Fe dendrite region.

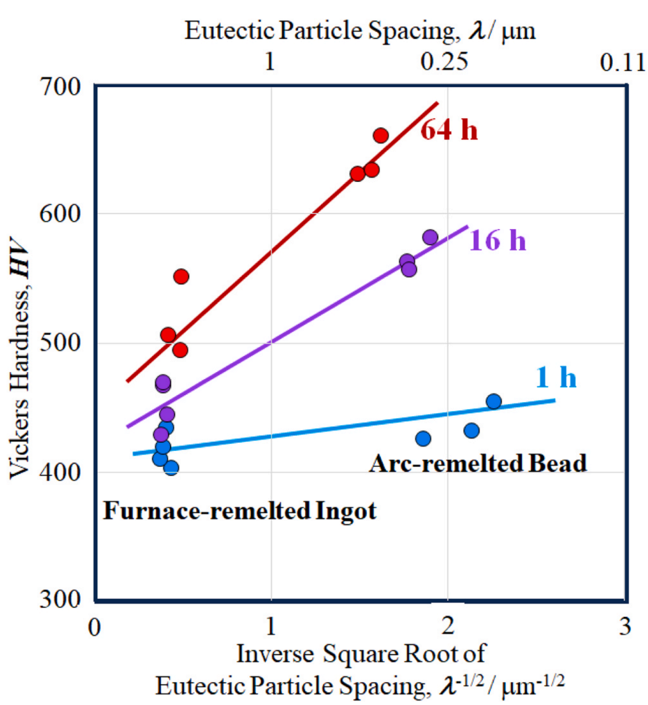

Fig. 11. Effects of eutectic particle spacing and holding time at 800 °C on hardness of the furnace-remelted ingot samples and the arc-remelted bead samples.

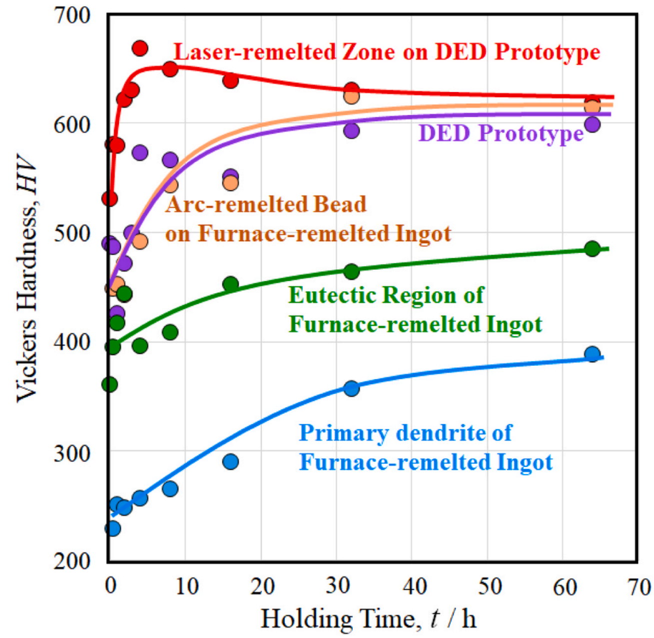

Fig. 12. Effects of holding time at 800 °C on hardness of different samples fabricated by different processes.

4. Conclusions

An Fe-C-Cr-Ni hypoeutectic alloy powder with a composition of Fe-2.14mass%C-32.38mass%Cr-6.48mass%Ni-0.90mass%Si was produced, and five types of samples were fabricated from this powder at five different cooling rates ranging from 2×10^{-1} to $\sim 10^{7}$ °C/s. The effects of dendrite arm spacing and eutectic particle spacing on the hardness of the as-solidified samples were investigated, as well as the precipitation hardening behavior of the samples during post-heat treatment at 800 °C. The results indicated that the present alloy exhibited considerably high hardness when rapidly solidified, similar to additive manufacturing processes such as laser powder bed fusion process and directed energy deposition process, and that post-heat treatment was effective in further hardening the additive manufacturing products. The individual conclusions are presented in more detail below.

(1) The hardness of the as-solidified samples increased exponentially with decreasing γ-Fe dendrite arm spacing and eutectic Cr_7C_3 particle spacing, with the latter effect being stronger than the former.

(2) A nearly proportional relationship was observed between the inverse square root of eutectic particle spacing and the hardness of the heat-treated samples, indicating that the Hall-Petch law still applies to this hypoeutectic alloy even after heat treatment at 800 °C.

(3) During heat treatment, extremely fine $Cr_{23}C_6$ particles precipitated in both the Fe dendrite arms and the Fe matrix of the eutectic region, increasing the hardness of the alloy samples. The increase in hardness during heat treatment was greater with higher cooling rates during sample solidification. This is because higher cooling rates increase the degree of supersaturation of alloying elements, leading to higher nucleation frequency of precipitates and consequently to enhanced precipitation hardening.

CRediT authorship contribution statement

Naomi Kitagawa: Investigation. **Norihito Sakaguchi:** Investigation, Funding acquisition. **Genki Saito:** Investigation. **Dariusz Kata:**

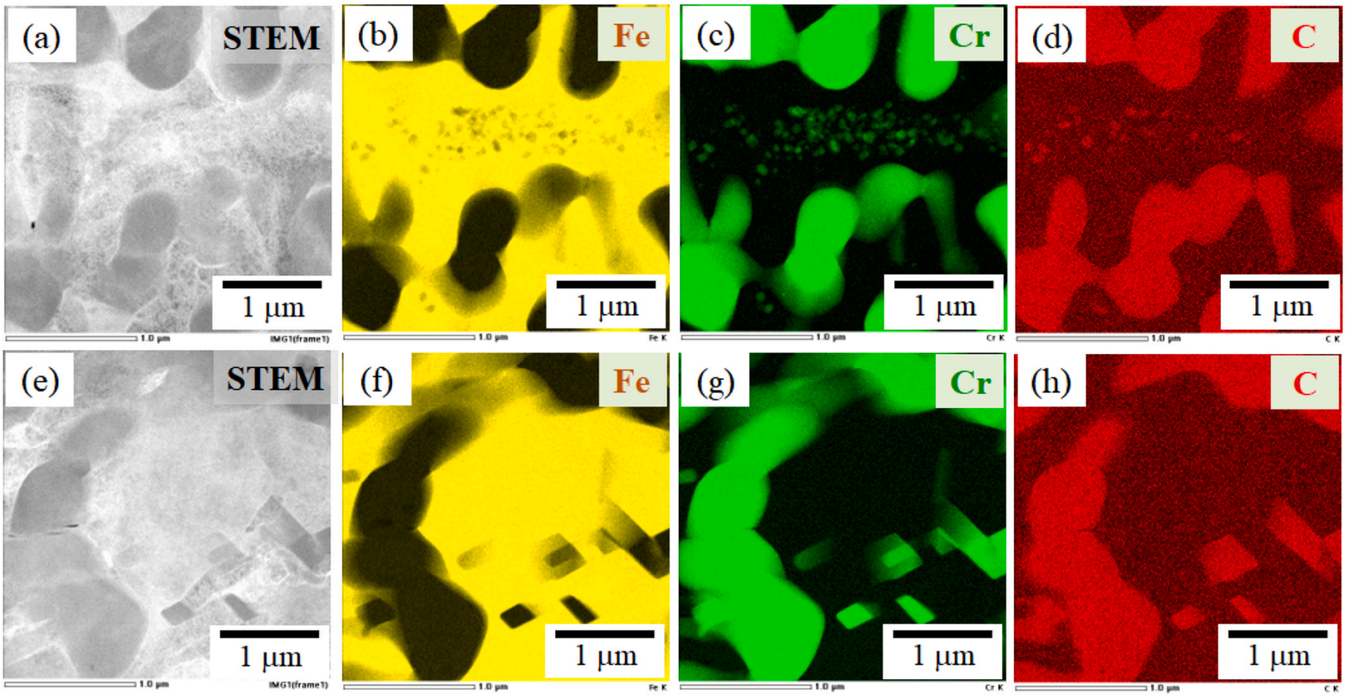

Fig. 13. STEM-EDS analysis results of (a-d) the laser-remelted zone and (e-h) the DED prototype, showing fine chromium carbide precipitates in the γ-Fe dendrite arms and Ostwald-ripen coarse eutectic chromium carbide particles in the inter-dendritic region, after heat-treated for 32 h at 800 ^{o}C.

Writing – review & editing. **Rutkowski Paweł:** Investigation. **Kiyotaka Matsuura:** Writing – review & editing, Writing – original draft, Supervision, Methodology, Investigation, Conceptualization.

Declaration of Competing Interest

The authors declare the following financial interests/personal relationships which may be considered as potential competing interests: Norihito Sakaguchi reports financial support was provided by Hokkaido University Faculty. Kiyotaka Matsuura reports a relationship with Mitsubishi Steel Mfg Co Ltd that includes: consulting or advisory. Kiyotaka Matsuura has patent Production method of a stainless steel pending to assignee. If there are other authors, they declare that they have no known competing financial interests or personal relationships that could have appeared to influence the work reported in this paper.

Acknowledgements

The authors would like to thank Yukiko Tanaka, MSc, Emiko Obari, BSc, and graduate student Ikunosuke Miyasaka of Department of Materials Science of Faculty of Engineering, Hokkaido University. Arc-remelting was performed at Hokkaido Bureau Welding Engineering Evaluation Committees of The Japan Welding Engineering Society. Directed energy deposition of the prototype was performed at AeroEdge Co., Ltd. Laser powder bed fusion of the small prototype was performed at Washin Sangyo Co., Ltd. This research was partially supported by "Advanced Research Infrastructure for Materials and Nanotechnology in Japan (ARIM)" of the Ministry of Education, Culture, Sports, Science and Technology (MEXT) at Hokkaido University.

References

[1] T. Murakumo, T. Kobayashi, Y. Koizumi, H. Harada, Creep behaviour of Ni-base single-crystal superalloys with various γ′ volume fraction, Acta Mater. 52 (12) (2004) 3737–3744, https://doi.org/10.1016/j.actamat.2004.04.028. ⟨https://www.sciencedirect.com/science/article/pii/S1359645404002447⟩.

[2] I.G. Akande, O.O. Oluwole, O.S.I. Fayomi, O.A. Odunlami, Overview of mechanical, microstructural, oxidation properties and high-temperature applications of superalloys, Mater. Today. Proc. 43 (2021) 2222–2231, https://doi.org/10.1016/j.matpr.2020.12.523. ⟨https://www.sciencedirect.com/science/article/pii/S2214785320402408⟩.

[3] T.M. Pollock, S. Tin, Nickel-based superalloys for advanced turbine engines: chemistry, microstructure and properties, J. Propuls. Power 22 (2) (2006) 361–374, https://doi.org/10.2514/1.18239. ⟨https://arc.aiaa.org/doi/abs/10.2514/1.18239⟩.

[4] E. Akca, A. Gürsel, A review on superalloys and IN718 Nickel-Based INCONEL superalloy, Period. Eng. Nat. Sci. (PEN) 3 (2015).

[5] K. Matsuura, G. Saito, N. Sakaguchi, N. Kitagawa, P. Rutkowski, D. Kata, Hall-Petch strengthening of an Fe-C-Cr-Ni eutectic alloy under additive manufacturing conditions, J. Alloy. Compd. 1043 (2025) 184213, https://doi.org/10.1016/j.jallcom.2025.184213.

[6] N. Soldevilla, O. Caballero, Correlation of secondary dendrite arm spacing with the mechanical behaviour of cast 718 alloy 8th International Symposium on Superalloy 718 and Derivatives, in: E. Ott, A. Banik, X. Liu, I. Dempster, K. Heck, J. Andersson, J. Groh, T. Gabb, R. Helmink, A. Wusatowska-Sarnek (Eds.), TMS (The Minerals, Metals & Materials Society), 2014. ⟨https://www.tms.org/superalloys/10.7449/2014/Superalloys_2014_757_768.pdf⟩.

[7] G. Liu, S. Winwood, K. Rhodes, S. Birosca, The effects of grain size, dendritic structure and crystallographic orientation on fatigue crack propagation in IN713C nickel-based superalloy, Int. J. Plast. 125 (2020) 150–168, https://doi.org/10.1016/j.ijplas.2019.09.010. ⟨https://www.sciencedirect.com/science/article/abs/pii/S0749641919303948?via%3Dihub⟩ (February, Pages).

[8] L. Wang, B. Ye, W. Huang, W. Ding, Theoretical model of yield strength for eutectic colony microstructure materials, Scr. Mater. 231 (2023) 115443, https://doi.org/10.1016/j.scriptamat.2023.115443. ⟨https://www.sciencedirect.com/science/article/pii/S1359646223001677⟩.

[9] L.E. Ramirez-Vidaurri, M. Castro-Román, M. Herrera-Trejo, K.L. Fraga-Chavez, Secondary dendritic arm spacing and cooling rate relationship for an ASTM F75 alloy, J. Mater. Res. Technol. 19 (2022) 5049–5065, https://doi.org/10.1016/j.jmrt.2022.06.146. ⟨https://www.sciencedirect.com/science/article/pii/S2238785422010080⟩.

[10] P.A. Hoope, Melt pool temperature and cooling rates in laser powder bed fusion, Addit. Manuf. 22 (2018) 548–559, https://doi.org/10.1016/j.addma.2018.05.032. ⟨https://www.sciencedirect.com/science/article/pii/S221486041830188X⟩.

[11] A. Kurdi, A. Aldoshan, F. Alshabouna, A. Alodadi, A. Degnah, H. Alnaser, T. Tabbakh, A.K. Basak, Investigation into the Microstructure and Hardness of Additively Manufactured (3D-Printed) Inconel 718 Alloy, 16, Materials (Basel) 16 (6) (2023) 2383, https://doi.org/10.3390/ma16062383, ⟨https://pubmed.ncbi.nlm.nih.gov/36984263/⟩, 16.